Available online at www.sciencedirect.com
ScienceDirect
Continental Shelf Research 28 (2008) 338–350
CONTINENTAL SHELF RESEARCH
www.elsevier.com/locate/csr

Tides and mixing in the northwestern East China Sea, Part II: Near-bottom turbulence

Iossif Lozovatsky[a,b,*], Zhiyu Liu[c], Hao Wei[c], H.J.S. Fernando[a]

[a]Department of Mechanical and Aerospace Engineering, Arizona State University, Environmental Fluid Dynamics Program, AZ 85287-8909, USA
[b]P.P. Shirshov Institute of Oceanology, Russian Academy of Sciences, Moscow 117997, Russia
[c]Physical Oceanography Laboratory, Ocean University of China, Qingdao 266100, PR China

Available online 14 September 2007

Abstract

The dissipation rate of turbulent kinetic energy ε and friction velocity u_* was studied in reversing and rotating tidal flows in the East China Sea near the northeastern coast of China using ADV and ADCP measurements. The highest near-bottom dissipation rate on a shallow (19 m depth) shelf $\varepsilon_{nb}\sim 5\times 10^{-5}$ W/kg was associated with the stronger flooding current of the reversing tide and the lowest $\varepsilon_{nb}\sim 10^{-7}$ W/kg with the weaker ebb current. The log-layer (ADCP-based) and the skin-layer (ADV-based) near-bottom estimates of friction velocities, $u_{*(\log)}$ and $u_{*(\mathrm{cor})}$, showed close correspondence for the reversing tidal flow, but when the tidal vector rotated over a sloping bottom $u_{*(\log)}$ was approximately two times larger than $u_{*(\mathrm{cor})}$. The inapplicability of the Prandtl–Karman log-layer scaling for energetic rotating flow is considered as the major source for this discrepancy. The classical wall-layer parameterization $\varepsilon_{nb}=c_0u_*^3/\kappa\zeta$ with $c_0=1$ was found to hold well for the reversing tide, but for rotating flow $c_0=1.5$. The scaling for the dissipation rate, $\varepsilon=c_\varepsilon e_{tr}^{3/2}/L_{tr}$, used in the turbulent kinetic energy (e_{tr}) balance equation requires $c_\varepsilon=0.06$ for the reversing tide, but $c_\varepsilon=0.09$ for the rotating flow, where the turbulent scale $L_{tr}=\kappa\zeta$ and ζ is the distance from the seafloor. Significant departure from the wall layer parameterization was noted when advection of warm water affected the testing site at a sloping shelf (38 m depth), possibly causing convective mixing in addition to boundary-induced turbulence.

Keywords: Tidal flows; East China Sea; Turbulence; Mixing; Friction velocity; Log-layer; Skin-layer

1. Introduction

Studies of small-scale dynamics in shallow tidal waters have made substantial progress recently due to the advent of a new generation of high-resolution, robust, high-sampling-rate acoustic doppler velocimeters (ADV) and acoustic doppler current profilers (ADCP and ADP). With ADVs, components of the near-bottom momentum stress ($-\overline{u'w'}$ and $-\overline{v'w'}$) and friction velocity $u_*=\sqrt{(-\overline{u'w'})^2+(-\overline{v'w'})^2}$ can be evaluated directly (Voulgaris and Trowbridge, 1998; Kim et al., 2000; Fugate and Chant, 2005), thus providing estimates of the drag coefficient $C_d=u_*^2/U^2$. This parameter is commonly used to formulate seafloor boundary conditions for numerical models of ocean circulation and in various engineering applications related to lakes, rivers, and reservoirs. Here U is a reference velocity, which is taken as either the mean velocity at a specified distance ζ above the seafloor, velocity averaged over the whole water column in shallow basins or a geostrophic velocity at the upper boundary of the bottom boundary layer (BBL). Friction velocities can also be inferred indirectly using ADCP velocity profiles (e.g., see Lueck and Lu, 1997; Friedrichs and Wright, 1997; Cheng et al., 1999; Foster et al., 2000; Elliott, 2002; Howarth and Souza, 2005) by fitting data to the Prandtl–Karman logarithmic layer velocity model $u(\zeta)=(u_*/\kappa)\log(\zeta/\zeta_0)$. Here ζ_0 is the aerodynamic roughness and $\kappa=0.4$ is the von Karman constant, and the assumption of a steady, unidirectional, fully developed parallel shear flow with weakly stable stratification is made. Measurements of the

*Corresponding author. Department of Mechanical and Aerospace Engineering, Arizona State University, Environmental Fluid Dynamics Program, AZ 85287-8909, USA.
E-mail address: i.lozovatsky@asu.edu (I. Lozovatsky).

0278-4343/$ - see front matter © 2007 Elsevier Ltd. All rights reserved.
doi:10.1016/j.csr.2007.08.007

kinetic energy dissipation rate ε at various heights ζ are also used to estimate u_* indirectly (e.g., Dewey and Crawford, 1988; Sanford and Lien, 1999; Shaw et al., 2001; MacKinnon and Gregg, 2005). This employs the law of the wall parameterization $\varepsilon = u_*^3/\kappa\zeta$, which assumes a simple local balance between shear generation $u_*^2\,\mathrm{d}\bar{U}/\mathrm{d}z$ and the dissipation ε of the turbulent kinetic energy $e_{tr} = \left(\overline{u'^2} + \overline{v'^2} + \overline{w'^2}\right)/2$. It has been shown that u_* obtained from the logarithmic fit to velocity profiles usually exceeds the ADV-based u_* (Friedrichs and Wright, 1997; Howarth and Souza, 2005), which has been attributed to the violation of underlying assumptions of the law of the wall parameterization (Smith and McLean, 1977; Li, 1994; Friedrichs and Wright, 1997). It is still unclear whether non-stationary local dynamics, stable stratification, details of bottom roughness and corresponding form drag or other factors are responsible for the disparity.

In this paper, small-scale dynamics of shallow tidal waters are studied in the northwestern sector of the East China Sea (ECS). ADCP and ADV data were obtained in reversing and rotating tidal flows. The instrument layout and basic meteorological conditions during the measurement campaigns were given in Lozovatsky et al. (2007), which will be referred to as LLWF-1 throughout the text. In Section 2, the major findings of LLWF-1 are summarized. In Section 3, the near-bottom dissipation rate ε_{nb} and diffusivities K_z and their dependence on the turbulent Reynolds number are discussed as well as the impact of possible convective mixing associated with advection of warmer water along the seafloor. In this section, we also present the layer-averaged dissipation rate $\langle\varepsilon\rangle$ and diffusivity $\langle K_z{\sim}L_{Th}^2N\rangle$ below the pycnocline (based on Dillon's (1982) linear correlation between the Thorpe L_{Th} and Ozmidov $L_N = \varepsilon^{1/2}/N^{3/2}$ scales) and analyze the dependence of these variables on the bulk Richardson number $Ri_b = \langle N^2\rangle/\langle Sh^2\rangle$, where $\langle N^2\rangle$ and $\langle Sh^2\rangle$ the squared buoyancy frequency and mean vertical shear, respectively. The variation of friction velocity in various tidal regimes is discussed in Section 4. The interplay among ε_{nb}, u_*, and e_{tr} in reversing (channeled) and rotating tidal flows is addressed in Section 5. The summary is given in Section 6.

2. Characteristics of rotating and reversing tidal flows: a summary of LLWF-1

In order to analyze the near-bottom turbulence in shallow-water tidal currents, data from bottom-mounted ADV and ADCP at two stations in ECS along the northeastern coast of China were used. The measurements were carried out on March 26–27, 2005 at St. **A1** (35.90°N, 121.58°E, the mean water depth $z_B = 38$ m) and on December 14, 2005 at St. **D** (36.04°N, 120.32°E, $z_B = 19$ m). Fig. 1 of LLWF-1 shows the bathymetry in the region and the station locations. An additional station,

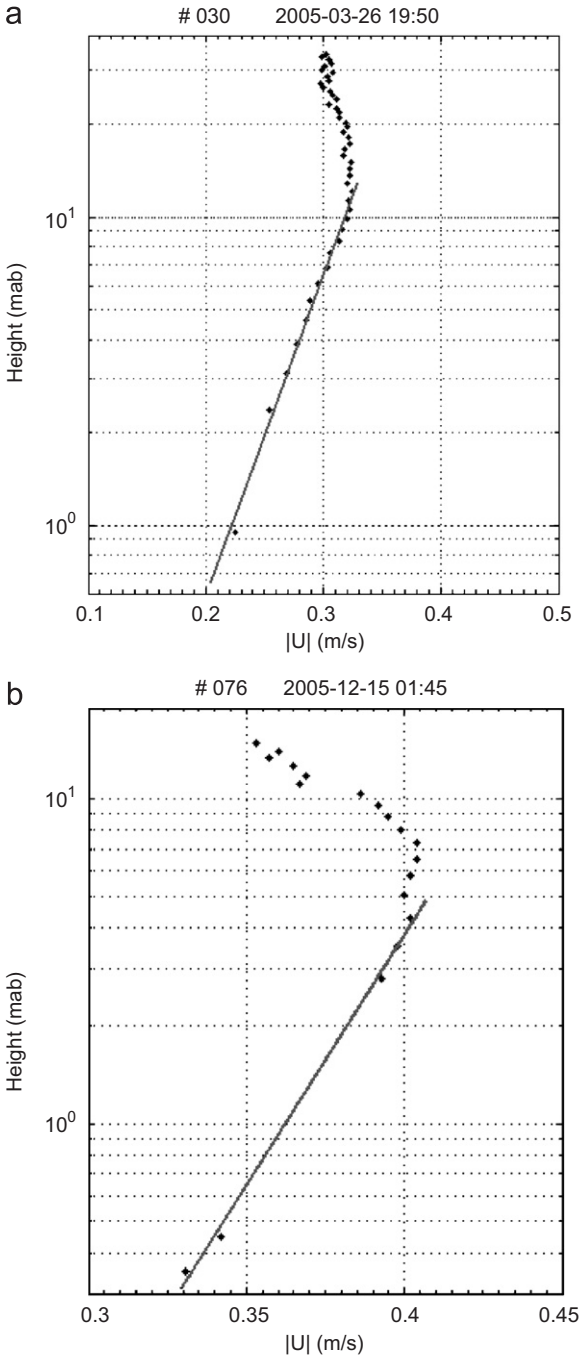

Fig. 1. Examples of the velocity profiles $U(\zeta)$ at St. **A1** (a) and St. **D** (b) exhibiting evident logarithmic boundary layers (straight line approximation) to a height of $H_l{\sim}10$ and 4–5 mab, respectively.

St. **A2** (March 20–21: 38.50°N, 123.00°E, $z_B = 58$ m), was used only for the analysis of temporal variations of thermohaline and velocity structure. A 6 MHz Nortek "Vector" ADV and a 600 kHz RDI 4-beam Jenus ADCP were employed for a 25-h period (over two semidiurnal tidal cycles) at each station. The height of the upward looking ADV sampling volume at the St. **A1** was set up at $\zeta_s = 0.95$ mab (meters above the bottom). For the downward looking ADV at shallower St. **D** $\zeta_s = 0.45$ mab. A 10-min sampling cycle was used for data collection at

St. **A1** with a 64 Hz sampling rate over 32 s of each burst. At St. **D**, the ADV sampling rate was 16 Hz but the data were recorded continuously. The vertical resolution of ADCP profiles $u(\zeta)$, $v(\zeta)$, and $w(\zeta)$ was 0.75 m through the whole water column. The closest to the seabed level of ADCP measurements at St. **A1** was at $\zeta = 2.4$ mab and $\zeta = 2.8$ mab at St. **D**.

A semidiurnal barotropic tide with a slightly stretched ellipse of the counter-clockwise rotating current vector was observed at St. **A1**. At St. **D**, a nearly unidirectional reversing tidal flow dominated. The M_2 amplitude of the west-directed flood current of 0.4 m/s was twice that of the east-directed ebb current. The characteristic amplitudes of the M_2 constituent were 0.35 m/s at St. **A1** and 0.42 m/s at St. **D**, respectively. The reversing tidal flow at St. **D** was affected by seiches of ~2.3 h period generated in semi-enclosed Jiaozhou Bay (JB) located nearby. Seiching modulation of zonal velocity during the ebb tide was comparable with the tidal amplitude. Records of vertical velocity in weakly stratified layer between the pycnocline and the seafloor at St. **A1** showed signatures of internal semidiurnal tide as well as quasi-sinusoidal fluctuations close to intrinsic frequency (τ_{iw}~50 min) that can be attributed to internal waves. The beam angle of tidal internal-wave energy s_{TIW} is in the range 0.023–0.035, which substantially exceeds the local bottom slope α_b. The energy of internal tide therefore may propagate upslope on-shelf but it cannot be accumulated at the testing site.

At the sloping shelf (St. **A1**), the upper boundary of the logarithmic layer H_l, which was usually coincided with the velocity maximum U_{max} in $U(\zeta)$ profiles, varied with approximately M_4 period in the range 6–15 mab. The log-layer at shallower St. **D** occupied ~4–5 mab (see examples in Fig. 1). The high-shear zones, which generated with the M_4 period at the seafloor extended across the whole water column in rotating tidal flow at St. **A1**. This specific feature might be associated with the upward propagation of the near-bottom-generated shear up to H_l and distorted above this layer due to the periodic increase and decrease of $U(\zeta)$ toward the sea surface. The time lag between the shear generation in BBL and at the upper levels produced an almost permanent slope of ~5 m/h in a time-depth shear section. Substantially, different patterns of shear between rotating tidal flows (St. **A1**) and reversing tidal currents (St. **D**) may influence near-bottom turbulence and mixing in different regions of ECS in a different way.

3. Dissipation and eddy diffusivity

The ADV data allow the estimation of the kinetic energy dissipation rate ε at $\zeta = 0.95$ mab (St. **A1**) and 0.45 mab (St. **D**) calculating spectral densities of the velocity fluctuations u', v', and w' and identifying the inertial subrange (Kolmogorov, 1941)

$$E_{u_i}(\kappa) = \alpha_{u_i}\tilde{\varepsilon}^{2/3}\kappa^{-5/3}, \tag{1a}$$

if it exists. Here u_i is u', v', and w' for $i = 1, 2, 3$, respectively (u' and v' are the fluctuations of horizontal components along and normal to the mean flow), $\tilde{\varepsilon}$ the dissipation rate averaged over the inertial subrange, and κ is the wavenumber. The Kolmogorov constant for one-dimensional spectra are $\alpha_u = 0.5$ for $E_u(\kappa)$ and $\alpha_v = \alpha_w = 4/3\alpha_u = 0.67$ for $E_v(\kappa)$ and $E_w(\kappa)$ (Monin and Yaglom, 1975; Green, 1992; Sreenivasan, 1993). Because the ADV data are point measurements, Taylor's "frozen turbulence" hypothesis was employed to transform the frequency spectra $E(f)$ to the wavenumber spectra $E(\kappa)$, viz.

$$E_{u_i}(f) = \left(\frac{\bar{U}}{2\pi}\right)^{2/3}\alpha_{u_i}\tilde{\varepsilon}^{2/3}f^{-5/3}. \tag{1b}$$

The dissipation rate $\tilde{\varepsilon}$ can be estimated from Eq. (1b) for relatively short segments of approximately constant mean velocity $\bar{U}$, an approach that has been used in a number of studies on near-bottom turbulence in the presence of strong tidal currents (e.g., Kim et al., 2000; Doron et al., 2001; Smith et al., 2005).

It has been reported (Stapleton and Huntley, 1995) that spectra of vertical velocity $E_w(f)$ from bottom-mounted ADVs have a lower noise level at higher frequencies compared to those of u' and v', which was the case in our measurements. Fig. 2a shows examples of a wide-range frequency spectra $E_u(f)$, $E_v(f)$, and $E_w(f)$ for St. **D** for a time interval corresponding to unidirectional flood tidal flow (see Fig. 4; $t = 7{:}11$–$9{:}19$). The spectral densities of all velocity components exhibit a relatively wide "$-5/3$" inertial subrange, which, as expected (Monin and Yaglom, 1975), is wider in $E_u(f)$ compare to $E_w(f)$. On the other hand, at high frequencies, spectra of horizontal components are affected by noise at lower f ($f > 2$–3 Hz). The energy preserving spectra $fE_u(f)$ and $fE_w(f)$ are shown in Fig. 2b emphasize the higher level of high-frequency noise for $E_u(f)$. A spectral maximum at f~0.12 Hz (τ~8 s) is conceivably related to the energy input from surface waves. Therefore, only $E_w(f)$ spectra were used to calculate the dissipation rate.

Because of 10-min burst-sampling of the ADV data at St. **A1** (2048 samples in each burst), 147 higher frequency ($f > 0.1$ Hz) spectra $E_w(f)$ were computed and inertial subrange was not evident only in eight spectra. Several examples of $E_w(f)$ are given in Fig. 3 (spectra with local maxima at $f = 2$–3 Hz will be discussed later).

Since continuous ADV records were available for St. **D**, it was possible to compute $E_w(f)$ at various time intervals. To obtain $\tilde{\varepsilon}$ with the averaging scale close to the time scale that was used for St. **A1**, $E_w(f)$ were calculated at 1-min segments (due to a lower sampling rate than at St. **A1**) with 10 min shift. The corresponding $E_w(f)$ obtained for St. **D** were similar to those in Fig. 3, but none of them exhibited confident spectral maximum at $f > 0.5$ Hz.

The near-bottom dissipation rate ε_{nb} at St. **D** is shown in Fig. 4 with five-point running averaging. Variations of ε_{nb} at hourly scales are similar to the variations of the

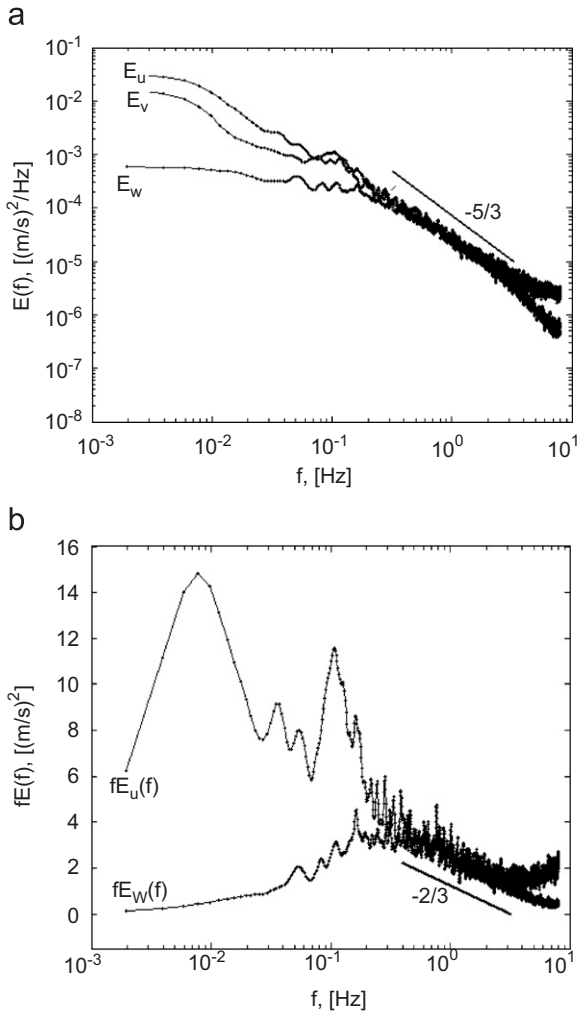

Fig. 2. (a) Wide-range spectral densities of ADV velocity components exhibiting the "−5/3" inertial subrange (St. **D**, $t = 7{:}11$–$9{:}19$ h; flood tidal current) and (b) the energy preserving spectra of the longitudinal u and vertical w components.

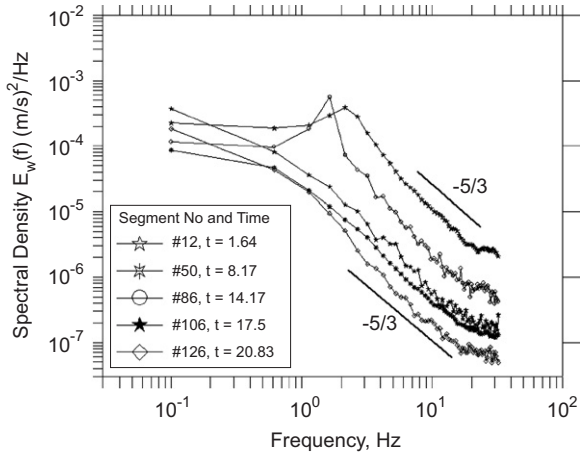

Fig. 3. St. **A1**: examples of spectral densities $E_w(f)$ showing a relatively wide "−5/3" inertial subrange. The segment numbers and time (from 15:00 LT; March 26, 2005) are given in the legend (corresponding ε are shown in Fig. 4). Spectra with local maxima are related to the tidal phase where the direction of tidal current changes from upslope to down-slope (see Fig. 5).

near-bottom turbulent Reynolds number $Re_{nb} = (\Delta U/\zeta_s)L_{tr}^2/\nu$, where ΔU is the ADV velocity at $\zeta_s = 0.45$ mab (thus $U_{\zeta=0} = 0$), L_{tr} is the characteristic turbulence scale, and ν is the molecular viscosity. Near the seafloor, the velocity profiles often exhibited the logarithmic layer

$$U(\zeta) = \left(\frac{u_*}{\kappa}\right)\log\left(\frac{\zeta}{\zeta_0}\right), \tag{2}$$

and therefore the turbulence scale can be expressed as $L_{tr} = \kappa\zeta$, using which the Re_{nb} was estimated to be in the range $\sim 10^2$–10^3, with the highest values occurring during west-directed inflows to **JB** (see the flow direction ϕ^o in Fig. 4). The dissipation rate increases up to 5×10^{-5} W/kg during the flood tide ($t \sim 10$–11 and $t \sim 22$–23 in Fig. 4) and it goes down to $\sim 10^{-7}$ W/kg during the ebb tide ($t \sim 5$ and 17). Modulation of the weak east-directed ebb flow by seiches generated in **JB** (see Fig. 1 and discussion in LLWF-1) is responsible for periodic increase of Re_{nb} and ε_{nb} during the ebb tide with seiche-related period of ~ 2 h ($t = 13$–18 and $t = 2$–4 in Fig. 4).

It is of interest to estimate the turbulent diffusivity near the bottom, which can be defined, for example, in terms of the Richardson diffusion coefficient $K_{nb} = a\varepsilon^{1/3}L_{tr}^{4/3}$ (Monin and Yaglom, 1971). Assuming $a = 1$ and $L_{tr} = \kappa\zeta = 0.18$ m, the near-bottom diffusivity $K_{nb} \approx 3 \times (10^{-4}$–$10^{-3})$ m^2/s, which is relatively low compared to the tidal channel flows (Friedrichs and Hamrick, 1996). To test the choice of L_{tr} parameterization, we also employed $L_{tr} = 0.5(w')^3/\varepsilon$ (Monin and Yaglom, 1975), where (w') was estimated as $rms(w')$ at 1-min segments. Diffusivities for both L_{tr} scalings are given in Fig. 4, showing a close match. Here the coefficient of linear regression through origin was 0.995 and the coefficient of determination $r^2 = 0.94$. This implies that a constant outer scale at a specific height above the bottom works reasonably well, irrespective of the direction and magnitude of tidal vector. This also substantiates the assumption that the logarithmic layer at St. **D** represent the layer of constant momentum flux in reversing (channeled) tidal flow rather than being a fictitious log-layer reported in several studies (see Lorke et al., 2002). The friction velocity u_*, therefore, can be estimated with confidence using log-layer velocity profiles at St. **D**.

At St. **A1**, the flow rotates counterclockwise depicting a good semidiurnal tidal ellipse with the main axis in the NW–SE direction approximately across the isobaths (the aspect ratio is ~0.3 over 0.15 m/s, i.e. 2:1). The dissipation rate ε_{nb} here does not always correlate with tidally induced variations of Re_{nb} as it is the case for St. **D**. During two periods ($t = 0.6$–4.5 and $t = 13$–16.5) that are shaded in Fig. 5a, ε_{nb} is surprisingly out of phase with Re_{nb}, which could be related to the rotation of the flow vector, namely the change of its direction from upslope to down-slope (from $\phi^o \sim 300^\circ$ to 160°, which is from NW to SE). A high-level turbulence (maximum of ε) was generated when the tidal vector turned to the WSW along the slope ($\phi^o \sim 240^\circ$), at the same time having a relatively low flow magnitude

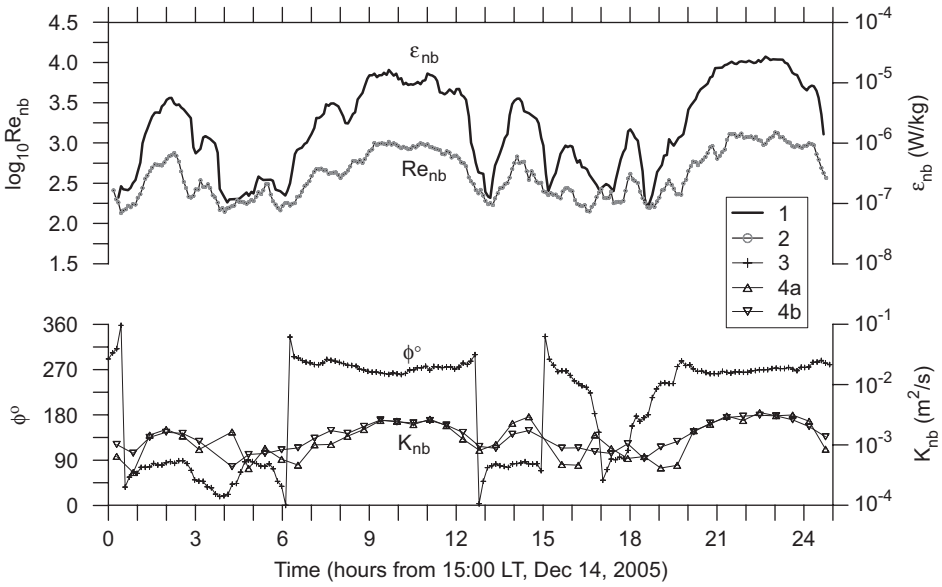

Fig. 4. St. **D**: the near-bottom dissipation rate ε_{nb} (1-min segments, five-point running averaging (1), the logarithm of turbulent Reynolds number Re_{nb} (2), direction of the mean flow ϕ^o (3), and the eddy diffusivity K_{nb} ((4a) for $L_{tr} = \kappa\zeta = 0.18$ m; (4b) for $L_{tr} = 0.5\,rms(w')^3/\varepsilon$).

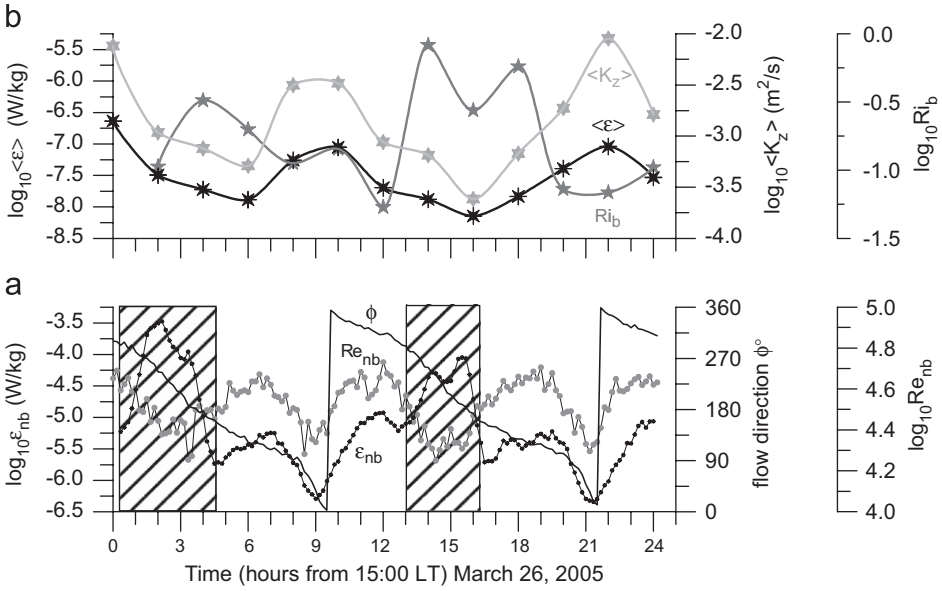

Fig. 5. St. **A1**: (a, lower panel) the logarithm of the near-bottom dissipation rate ε_{nb} and turbulent Reynolds number Re_{nb} and the direction of mean flow (ϕ^o) at $\zeta = 0.95$ mab; (b, upper panel) the logarithm of depth-averaged dissipation rate $\langle\varepsilon\rangle$, bulk Richardson number Ri_b, and vertical diffusivity $\langle K_z\rangle$ in the lower part of the water column below the pycnocline ($z = 20$–32 m). The shaded segments are the periods where the tidal vector turns from the upslope to down-slope.

and thus the lowest Re_{nb}. Time variations of vertical velocity induced near the seafloor by short-period internal waves (LLWI-1; Fig. 12a) do not show any specifics at two segments of enhanced ε_{nb}, and thus the possibility of local generation of high-level turbulence by internal waves is negligible. As has been mentioned in Section 2 (see also LLWF-1), the energy of semidiurnal internal tide at St. **A1** may propagate on to the shelf (Eriksen, 1982; Thorpe, 1987) because the angle of the energy beam $s_{TIW} =$ 0.023–0.035 is more than twice of the local bottom slope α_b. Therefore, no additional accumulation of internal-wave energy is possible onsite (as it would be for $s_{TIW} = \alpha_b$) to produce extra turbulence, which translates to a higher ε, above the level determine by tidally induced local Re_{nb}. Note that s_{TIW} approaches the critical condition $s_{TIW} = \alpha_b$ about 100 km NE from St. **A1**, near the tip of Shangdong Peninsula, where the slope angle $\alpha_b \sim 0.02$ and therefore the wave energy could be trapped and transferred to turbulence. Such remote source of near-bottom turbulence cannot affect ε at St. **A1**, although the

direction of turbulent kinetic energy advection is favorable (from NE).

It appears that the maxima of ε_{nb} observed during two periods of low Re_{nb} ($t\sim2$ and 15 in Fig. 5a) are well correlated with the M_2 tidal maxima of the near-bottom temperature (see T_{nb} for **A1** in Fig. 9 of LLWF-1). This indicates that in a specific phase of tidal rotation the along slope flow from the E–NE brings warmer near-bottom water to the testing site. This may trigger convective mixing, increasing ε_{nb} above the typical level associated with pure bottom friction. Note hat tidally driven near-bottom convection on a sloping seafloor has been reported by Moum et al. (2004). During the episodes of high ε_{nb}—low Re_{nb}, spectra of vertical velocity exhibit a confident maximum at $f=2$–4 Hz (see examples in Fig. 3). The amplitude of this maximum in consecutive spectra gradually grows as the flow rotates from the upslope to along slope (at $t=2$–3 and $t=14$–15). Then the spectral maximum becomes weaker and finally fades away (at the end of the marked segments in Fig. 5a) when the flow turns south, bringing cold near-shore water to the testing site. Therefore, the convection ceases, leaving behind regular drag-related bottom turbulence, with ε_{nb} and Re_{nb} varying in-phase. The observed spectral maxima ought to be associated with relatively high-frequency (2–4 Hz) oscillations of vertical velocity with spatial scales on the order of several centimeters (3–7 cm), which pertains to characteristic convective elements such as thermals and plumes.

The near-bottom diffusivity K_{nb} (not shown in the figure) was calculated using the law of the wall turbulent scale ($L_{tr}=\kappa\zeta=0.38$ m at $\zeta=0.95$ mab). It follows, as expected, the variations of Re_{nb} and ε_{nb} in segments without shading in Fig. 5a being in the range $(2-5)\times10^{-3}$ m^2/s. These are about an order of magnitude larger than the diffusivities estimated at the shallow non-tidal shelf of the Black Sea (Lozovatsky and Fernando, 2002). At the shaded segments, where convective mixing is perceived to be present, such K_{nb} estimates are unreliable as they are relevant only for shear-generated turbulence.

The lower part of the water column ($z>12$–15 m) at St. **A1** was not completely homogeneous, but weakly stratified (see LLWF-1). Thus, an attempt was made to estimate the dissipation and diffusivity in the water interior by calculating the Thorpe scales L_{Th} (Thorpe, 1977) and assuming $K_z=L_{Th}^2N$. The latter follows the Osborn–Cox formula for diffusivity $K=\gamma(\varepsilon/N^2)$ and Dillon's (1982) linear correlation between L_{Th} and the Ozmidov scale $L_N=\varepsilon^{1/2}/N^{3/2}$, which yields $\varepsilon=c_D^2L_{Th}^2N^{-3}$. Here, $c_D=0.8$, and γ is the mixing efficiency (see, for example, Thorpe (2005) for details). The Thorpe displacements d' were obtained from the 5 cm vertical resolution temperature profiles. The Thorpe scales $L_{Th}=rms(d')$ were calculated at each 1-m segment as well as local N^2, which was obtained after sorting the averaged density profiles. The individual 1-m estimates of ε and K_z were averaged over the entire depth range between the lower boundary of the thermocline and the end-points of profiles ($z\sim12$–37 m). In addition, the averaged squared shear $\langle Sh^2\rangle$ was calculated using the ADCP data, which along with the averaged squared buoyancy frequency $\langle N^2\rangle$ allowed estimation of the bulk Richardson number $Ri_b=\langle N^2\rangle/\langle Sh^2\rangle$ for each profile. The results of these calculations are shown in Fig. 5b. Although the time step between the samples (profiles) was very large (2 h), the averaged dissipation $\langle\varepsilon\rangle$ and diffusivity $\langle K_z\rangle$ exhibited variations representative of tidal origin (because of the sparse resolution, only scant effect of M_2 variations can be seen). The observed ranges are $\langle\varepsilon\rangle\sim10^{-8}$–$10^{-7}$ W/kg and $\langle K_z\rangle\sim2\times10^{-4}$–$6\times10^{-3}$ m^2/s. At times of high $\langle\varepsilon\rangle$ and $\langle K_z\rangle$ ($t=8$–10 and $t=21$), the bulk Richardson number is low, $Ri_b>0.1$, rising to $Ri_b\sim1$ when $\langle\varepsilon\rangle$ and $\langle K_z\rangle$ reaches their minima ($t=14$–18), which corresponds to strong domination of stratification (Strang and Fernando, 2001). This clearly points to the shear instability as a source of turbulence in the water interior between the pycnocline and the BBL. As has been discussed in LLWF-1, most probably the interior shear at St. **A1** is of tidal origin, generated above the log-layer due to the time dependent increase and decrease of horizontal velocity toward the sea surface. The time delay between the shear generated at different depths is almost constant across the water column, ~5 m/h. As such, turbulence appearance at the mid-depth of the interior layer ($z\sim22$–25 m, $\zeta\sim13$–16 mab) is expected to delay for ~3 h relative to that at the sea floor. This phase shift can be seen in Fig. 5b, (albeit because of the coarse resolution $\langle\varepsilon\rangle$ it is not striking). The maxima of Re_{nb} and ε_{nb} at $t=7$ correspond to the maxima of $\langle\varepsilon\rangle$ at $t=10$. Also compare the max(Re_{nb} and ε_{nb}) at $t=19$ with max($\langle\varepsilon\rangle$) at $t=22$, and min(Re_{nb} and ε_{nb}) at $t=13$ with min($\langle\varepsilon\rangle$) at $t=16$. The maxima of ε_{nb} at $t=2$ and 15 are not relevant for the comparisons because, as has been argued above, they are probably associated with convective turbulence rather than shear.

4. Friction velocity

The majority of velocity profiles at both stations **A1** and **D** depict a logarithmic layer above the seafloor with a characteristics thickness of several meters, and thus the friction velocities u_* and the aerodynamic roughness ζ_0 can be obtained by fitting individual velocity profiles to Eq. (2). Conversely, u_* can be estimated via ADV measurements of $-\overline{u'w'}$ and $-\overline{v'w'}$ (Kim et al., 2000; Souza and Howarth, 2005). Many authors (e.g., Friedrichs and Wright, 1997; Foster et al., 2000; Lorke et al., 2002) have expressed concern of using log-layer estimates for friction velocity considering that $u_{*(\log)}$ so obtained are usually (and sometimes significantly) larger than ADV-based friction velocity $u_{*(\mathrm{cor})}$, which is supposed to be influenced by the bottom stress (the so-called the skin-layer u_*). Howarth and Souza (2005) suggested that $u_{*(\log)}$ may represent processes of larger-scale than turbulence captured by ADV. Form drag, caused by sand ripples or other topographic inhomogeneities, has been offered as a source for higher

$u_{*(\log)}$ compared to $u_{*(\mathrm{cor})}$ given that it is added to the pure bottom stress (Smith and McLean, 1977; Chriss and Caldwell, 1982; Dewey and Crawford, 1988; Li, 1994; Lueck and Lu, 1997; Sanford and Lien, 1999). It is also possible (Lorke et al., 2002) that the log-layer observed is swayed by factors, which are not related to the wall-layer similarity laws. Friedrichs and Wright (1997) and Perlin et al. (2005) showed that even a small stratification in BBL could lead to an erroneous increase of friction velocity $u_{*(\log)}$ beyond the real value. In all, the mismatch between $u_{*(\log)}$ and $u_{*(\mathrm{cor})}$ is an issue of continuing interest.

Our calculations of u_* at St. **D** and St. **A1** also led to substantially different conclusions about the log-layer and skin-layer friction velocities. Variations of $u_{*(\mathrm{cor})}$ (ADV) and $u_{*(\log)}$ (ADCP) at St. **D** are shown in Fig. 6 along with the magnitude of the mean current U. Most of the time, both estimates are the same, particularly during the periods of unidirectional flood flow (compare with Fig. 4 where the flow direction is given). In the ebb phase, when the tidal current was superimposed by higher-frequency seiches-related oscillations (LLWF-1), the correlation between the two u_* estimates is weaker. Note that at 20 out of 30 segments between $t = 15$ and 20, the log-layer was undetectable. A regression plot made for 125 pairs of 10-min averaged samples of u_* (Fig. 7) yielded $u_{*(\mathrm{cor})} = 0.89u_{*(\log)}$ with $r^2 = 0.94$. If only those pairs of u_* pertained to the flooding phase, were used for regression (60 samples at $t = 6.5$–12.5 and $t = 20$–24), then $u_{*(\mathrm{cor})} = 0.93u_{*(\log)}$ with $r^2 = 0.97$. It appears that $u_{*(\log)}$ is still slightly larger than $u_{*(\mathrm{cor})}$, as has been reported in most previous studies and may in fact signify the nature of boundary layer turbulence over irregular topography. Note, however, that for high Reynolds number geophysical flows, the value of the von Karman constant can be taken as $\kappa = 0.35$ (Businger et al., 1971; Telford and Businger, 1986), which may further reduce the difference between $u_{*(\log)}$ and $u_{*(\mathrm{cor})}$. As such, the difference (less than 10%) between the two estimates of friction velocity at St. **D** may not be considered as statistically significant, when numerous uncertainties related to the measurements, length of records, variation of κ, and methods of calculation are taken into account.

Using $u_{*(\mathrm{cor})}$ and U, the drag coefficient $C_d = u_*^2/U^2$ was calculated, which is shown in Fig. 6. The median and standard deviation of C_d are 1.65×10^{-3} and 1.2×10^{-3}, respectively. It is important to emphasize that C_d is approximately constant, close to its median value, during

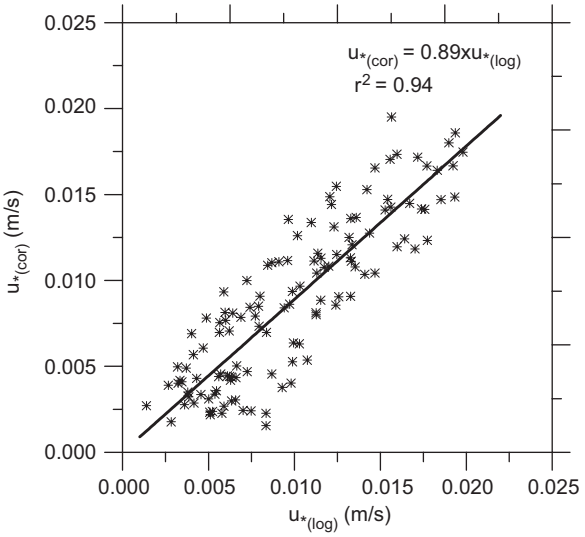

Fig. 7. Regression plot between $u_{*(\log)}$ (ADCP profiles) and the near-bottom $u_{*(\mathrm{cor})}$ (ADV data) friction velocities at St. **D**.

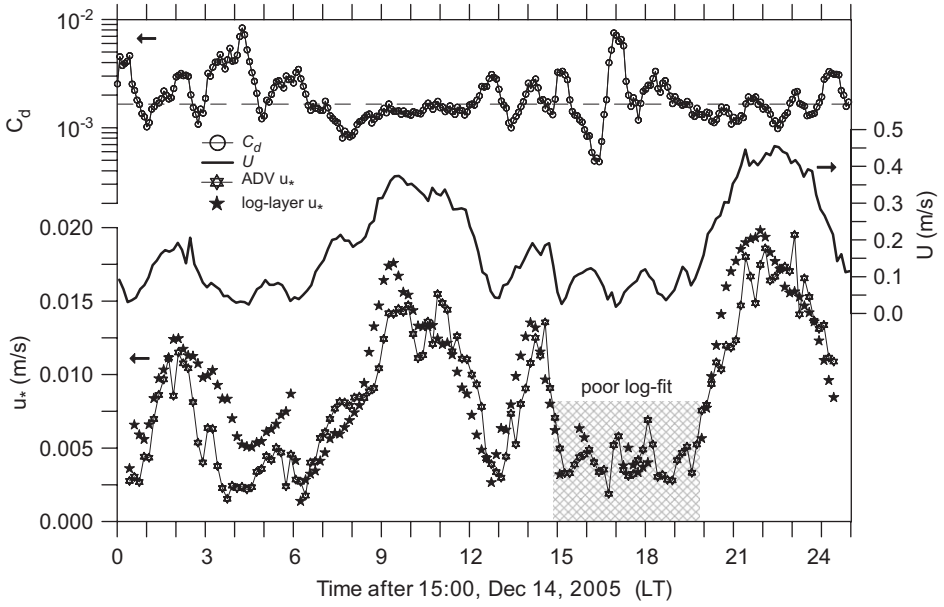

Fig. 6. St. **D**: the ADV and ADCP friction velocities (10-min time averaging) and the magnitude of the tidal current U (the tidal direction is shown in Fig. 4). The drag coefficient $C_d = u_*^2/U^2$ is based on ADV data; the dashed line is the median of $C_d = 1.65 \times 10^{-3}$.

the periods of unidirectional flood flow. The characteristic hydrodynamic roughness ζ_0 in this flow is very low, less than 0.01 m, and thus the physical bottom roughness.

At St. **A1**, where the mean flow vector rotates depicting a wide tidal ellipse, $u_{*(\log)}$ appears to be a factor of 2 larger, on the average, compared to $u_{*(\mathrm{cor})}$, particularly in segments where time variations of u_* were almost in phase ($t = 8$–13 and $t = 20$–24). These are the periods where tidal flow was directed upslope to the N–NW (see Fig. 8 and compare with Figs. 4 and 1).

The factor of 2 difference between $u_{*(\log)}$ and $u_{*(\mathrm{cor})}$ is typical for flows over sandy ripples, which can be attributed to the form drag (Li, 1994; Sanford and Lien, 1999). More specifically, laboratory experiments with flume flow (Li, 1994) have shown that the stress partition model of Smith and McLean (1977) correctly predicts the ratio between the skin friction and total shear stress, which is a sum of skin and form drags. Li (1994) suggested an empirical formula for $u_{*(\mathrm{cor})}/u_{*(\log)}$ as a function of the so-called "flow ripple parameter" $u_{*(\log)}/h_r$, where h_r is the ripple height. For the most common range of $u_{*(log)}/h_r = 1 - 2\,\mathrm{s}^{-1}$, the ratio $u_{*(\mathrm{cor})}/u_{*(\log)}$ varied in a narrow range, 0.5–0.6. At St. **A1**, $u_{*(\log)} = 0.015$–0.025 m/s (see Fig. 8) and therefore $u_{*(\log)}/h_r = 1.5\,\mathrm{s}^{-1}$, assuming $h_r = 1$–2 cm, which is the typical height of ripples on the slope at the testing site. This indicates that $u_{*(\mathrm{cor})}/u_{*(\log)}$ must be close to 0.5, if $u_{*(\log)}$ was affected by the form drag. It is interesting that when the flow was directed mainly along the slope ($t = 1$–4 and $t = 13$–16), the possible influence of form drag on $u_{*(\log)}$ was less significant. For the flow from southwest ($t = 2$–3), the skin friction velocity and log-layer u_* were almost equal. During the same phase of the next tidal cycle ($t = 15$–16), $u_{*(\log)}$ was only slightly larger than $u_{*(\mathrm{cor})}$. Such temporal variations of $u_{*(\log)}$ could be associated with the orientation of asymmetric ripples or other irregularities of bathymetry (Testik et al., 2006).

Influence of stratification on the increase of $u_{*(\log)}$ compared to the skin-layer u_* was reported by Perlin et al. (2005) based on the measurements of currents and turbulence in rotating tidal flow at the Oregon shelf, ($H_l = 5$–20 m), where $u_{*(\log)}$ was more than twice than u_* measured below 3 mab. The authors suggested a modified formula for the log-layer velocity, which accounts for stratification closer to the upper boundary of the layer. The friction velocity deduced from the modified formula was 2.24 times lower in the median compared to the standard $u_{*(\log)}$. Thus, the form drag as well as weak, but appreciable $\overline{N} = (2 - 2.4) \times 10^{-3}\,\mathrm{s}^{-1}$ in a thick log-layer may cause an increase of the friction velocity deduced from Eq. (2) by a factor of 2.

In addition to stratification and form drag effects the very nature of rotating tidal flows may cause violation of underlying assumptions of Eq. (2). The simplest system of the momentum equations for non-stratified rotating tidal flow is

$$\frac{\partial u_{td}}{\partial t} - F_c v_{td} = -g\frac{\partial \xi_{td}}{\partial x} + \frac{1}{\rho}\frac{\partial \tau_x}{\partial z} \quad \text{and}$$
$$\frac{\partial v_{td}}{\partial t} + F_c u_{td} = -g\frac{\partial \xi_{td}}{\partial y} + \frac{1}{\rho}\frac{\partial \tau_y}{\partial z}, \tag{3}$$

where τ_x and τ_y are the components of momentum stress, u_{td} and v_{td} are current components of the major M_2 constituent of barotropic tide, ξ_{td} is the tidal-related surface elevation, and the Coriolis parameter at the latitude $\varphi = 32^\circ$N, is $F_C = 2\Omega \sin\varphi = 7.7 \times 10^{-5}\,\mathrm{s}^{-1}$. The amplitudes and phases of

$$u_{td} = u_{M_2} \sin(\omega_{td} t - \psi_u), \qquad v_{td} = v_{M_2} \sin(\omega_{td} t - \psi_v),$$
$$\text{and} \quad \xi_{td} = \xi_{M_2} \sin(\omega_{td} t - \psi_\xi), \tag{4}$$

calculated using Fang's (see LLWF-1) regional tidal model are: $u_{M_2} = 0.29$ m/s, $v_{M_2} = 0.18$ m/s, $\xi_{M_2} = 1.1$ m and

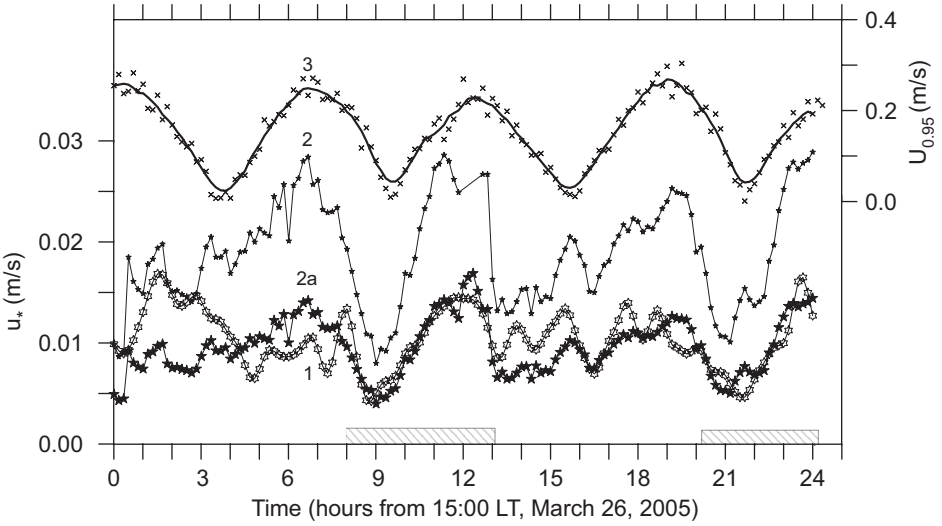

Fig. 8. St. **A1**: the ADV (1) and log-layer ADCP (2) friction velocities and the magnitude of mean current $U_{0.95}$ at $\zeta = 0.95$ mab (3); the solid line is $U_{0.95}$ with 1-h smoothing. The $(1/2)u_{*(log)}$ values are shown as (2a). The dashed segments along abscissa indicate the periods of upslope currents when a good match between (1) and (2a) can be seen.

$\psi_u = 244^\circ$, $\psi_v = 9^\circ$, and $\psi_\xi = 280^\circ$. The phase speed of the tidal wave (the semidiurnal tidal frequency $\omega_{td} = 1.41 \times 10^{-4}\,\mathrm{s}^{-1}$), if it is considered as a long Sverdrup plane wave, is $C_{td} = \sqrt{gH_b}(1 + F_c^2/\omega_{td}^2)^{1/2} = 22\,\mathrm{m/s}$, where $H_b = 38\,\mathrm{m}$ is the ocean depth (also see Beardsley et al., 2004). The horizontal gradients of the surface elevation can be estimated using tidal charts for the region produced by several numerical models (e.g., Guo and Yanagi, 1998; Kang et al., 2002). The tidal inversion software, OTIS, which utilizes the Topex/Poseidon altimetry data (Egbert and Erofeeva, 2002), was used to assess the amplitudes of the horizontal components of water elevation as $\hat{\xi}_x = 1.4 \times 10^{-6}$ and $\hat{\xi}_y = 2.6 \times 10^{-6}$, respectively. The characteristic values of the momentum stress components τ_x/ρ and τ_y/ρ in the BBL of height H_l, can be estimated from Eqs. (3) and (4) as

$$\frac{\tau_x}{\rho} = H_l(t)[u_{M_2}\omega_{td}\cos(\omega_{td}t - \psi_u) + F_c v_{td} + g\hat{\xi}_x \sin(\omega_{td}t - \psi_\xi)], \tag{5a}$$

$$\frac{\tau_y}{\rho} = H_l(t)[v_{M_2}\omega_{td}\cos(\omega_{td}t - \psi_u) - F_c u_{td} + g\hat{\xi}_y \sin(\omega_{td}t - \psi_\xi)], \tag{5b}$$

where $H_l(t)$ was specified as the upper boundary of the logarithmic layer, which approximately follow M_4 tidal variations (see Fig. 15 of LLWF-1). The estimates of the friction velocity $u_{*(M_2)} = [(\tau_x^2 + \tau_y^2)/\rho]^{1/2}$ deduced from Eqs. (5a) and (5b) resemble the main features of the log-layer friction velocity variations shown in Fig. 9. The maxima of $u_{*(M_2)}$, $\sim 2.2 \times 10^{-2}\,\mathrm{m/s}$, are consistent with maxima of $u_{*(\log)}$, $\sim (2.2\text{–}2.7) \times 10^{-2}\,\mathrm{m/s}$. The total tidal forcing that includes the Coriolis acceleration and horizontal pressure gradient appears to be responsible for the disparity between $u_{*(\mathrm{cor})}$, which apparently (Fig. 7) represents the momentum balance with constant flux, and $u_{*(\log)}$, which is not.

We can thus conclude that the use of formula based on constant momentum flux to estimate the friction velocity in a logarithmic-like, thick boundary layer is not correct because of the importance of the total momentum balance of rotating flows even during short periods (and not a component in the direction of the flow). There are also possible influences of form drug, and stratification. A combination of these effects leads to approximate two-times increase of $u_{*(\log)}$ compared with the skin-layer u_* obtained using flux correlation measurements (see Fig. 8).

5. The relationship between the dissipation and friction velocity

The dissipation parameterization for a wall-bounded stationary parallel shear flow takes the form

$$\varepsilon = c_0 \frac{u_*^3}{\kappa\zeta}, \tag{6}$$

where the c_0 is assumed to be unity and the von-Karman constant $\kappa = 0.4$. To validate Eq. (6) for reversing and rotating tidal currents we analyzed the bottom friction velocity and the dissipation rate (based on spectra of w') using ADV measurements at stations **D** and **A1**. As was shown in the previous section, the log-layer u_* at St. **D** correlated well with the ADV u_*, and thus it is not important which of the two estimates to be picked for evaluation. At St. **A1**, the two estimates of friction velocity are different and the use of Eq. (6), which is linked to logarithmic profiles, seems to be highly questionable. Eq. (6), however, may have general applicability here to the skin layer u_* since the ADV rms velocities are proportional to $u_{*(\mathrm{cor})}$ and lengthscales proportional to ζ. For St. **D**, where $\zeta = 0.45\,\mathrm{mab}$, Eq. (6) becomes $\varepsilon = 5.6 c_0 u_*^3$; for St. **A1**, where $\zeta = 0.95\,\mathrm{mab}$, $\varepsilon = 2.6 c_0 u_*^3$. A regression plot of ε versus u_* given in Fig. 10a shows that the dissipation rate ranges over four decades, and it is proportional to u_*^3. The best fit for St. **D** using 280 pairs of 1-min averaged samples (small dark circles) and Matlab

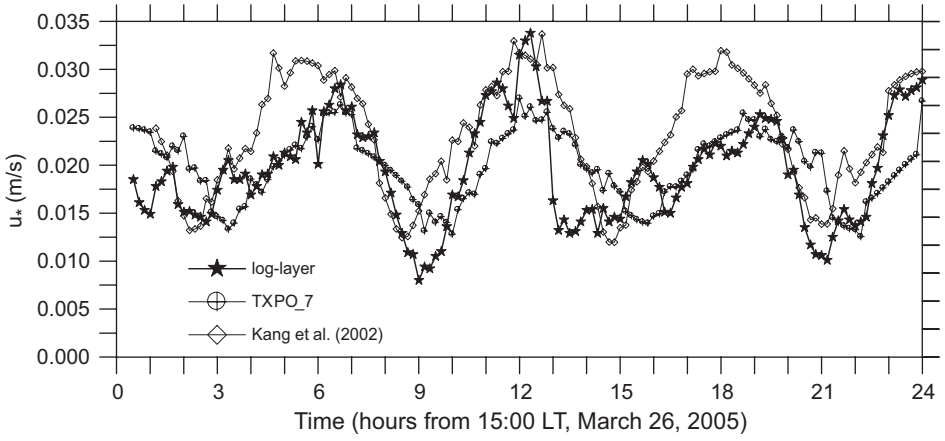

Fig. 9. The log-layer estimates of the friction velocity at St. **A1** (stars) and the estimates based on the total momentum balance of the barotropic tide in the point averaged over the height of log-layer using TPXO7.0 (Egbert and Erofeeva, 2002) and Kang et al. (2002) models.

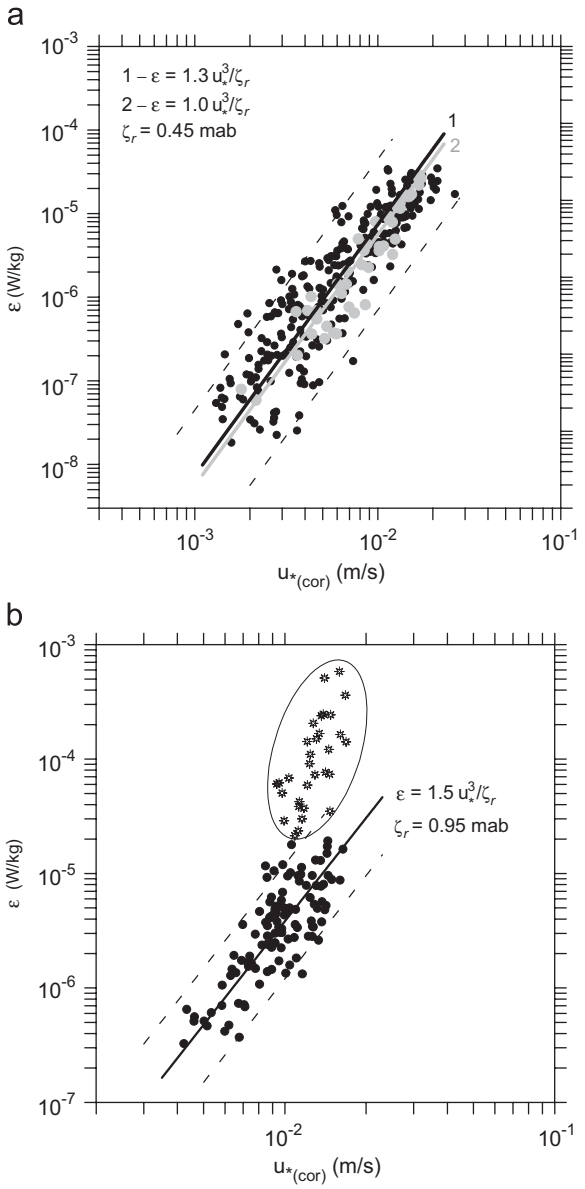

Fig. 10. The regression plots ε versus $u_{*(cor)}$ at St. **D** (a) and **A1** (b); see text for details.

curve fitting tool yielded $c_0 = 1.3$ (line 1), which is close to the classic value of unity. The 95% confidence bounds for this fit embrace almost all samples, which scatter around the regression line 1 over about one decade each side. If 30-min averaged estimates of ε and u_* are used (gray large circles), then $c_0 = 1$ (line 2). The results, therefore, supports the notion that the wall layer dissipation scaling is valid for reversing non-stratified tidal flows, which generally resemble channeled flows in estuaries and rivers.

An examination of the validity of Eq. (6) to the data taken at St. **A1** was also made (Fig. 10a and b). Recall, however, that the flow from the NE carries warmer bottom water (LLWF-1) favorable for convective mixing, we divided the total dataset of 144 samples of ε and $u_{*(cor)}$ into two subsets, based on segments shown in Fig. 5. Note that 133 samples were dominated by mechanical turbulence, which are shown in Fig. 10b by dark circles, and those, which were presumably influenced by convection (31 samples at the dashed segments in Fig. 5) are shown by open symbols. The best-fit line in Fig. 10b for dark circles gives $c_0 = 1.5$, which somewhat larger than 1. The range of ε in this case is less than two decades and the scatter around the best fit is uneven. Thus, it is unclear whether rotating tidal flow at a sloping bottom produces more turbulent kinetic energy (in addition to shear generation that is already accounted for u_*), or the higher $c_0 = 1.5$ simply implies insufficient statistics and standard uncertainties of measurements and data processing.

Dissipation values larger than 2×10^{-5} W/kg ($u_* \approx > 0.01$ m/s), which constitute data from the southwest directed flow, are almost independent of u_* with a jump of ε by almost two decades when u_* is increased simply by a factor of 2 (Fig. 10b, circled symbols). As discussed, this deviation from the law of the wall at St. **A1** can be attributed to convective turbulence produced by warmer water advected along the coast from northeast. Horizontal inhomogeneity of coastal waters at the slope is an essential factor influencing the near-bottom turbulence in ECS.

The ADV data allow also checking the relationship between the turbulent kinetic energy (TKE), e_t, and its dissipation ε, which is widely used to parameterize ε in the equation of the TKE balance as

$$\varepsilon = c_\varepsilon \frac{e_{tr}^{3/2}}{L_{tr}}, \tag{7}$$

where the turbulent scale $L_{tr} = \kappa\zeta = 0.18$ m at St. **D** and $L_{tr} = \kappa\zeta = 0.38$ m at St. **A1**. The traditional value of c_ε is in the range 0.06–0.12, the most often used being $c_\varepsilon = 0.08$ (e.g., Mellor and Yamada, 1982; Lozovatsky et al., 2006). The dependences of ε on e_{tr} are given in Fig. 11a and b for St. **D** and **A1**, respectively. The $\varepsilon \sim e_{tr}^{3/2}$ fits both data sets reasonably well. The corresponding $c_\varepsilon = 0.06$ for St. **D** ($r^2 = 0.88$) and $c_\varepsilon = 0.09$ for St. **A1** ($r^2 = 0.6$ for non-convective, bottom-stress induced turbulence). The both values are in the range usually assigned for c_ε in numerical models. Perhaps, rotating, weakly stratified flow (St. **A1**) requires about 50% larger c_ε compared to the reversing, almost homogeneous flow (St. **D**) in order to balance $\partial e_{tr}/\partial t$ only by viscous dissipation ε. At St. **A1**, however, part of the e_{tr} is utilized to work against the buoyancy force, which would add ~25% to c_ε based on standard mixing efficiency $\gamma = 0.2$. The anisotropy of turbulence in rotating flow at St. **A1** could also be more significant (affecting smaller scales of fluctuations) than that in reversing almost unidirectional flow at St. **D**. In that case, ε calculated using $E_w(f)$, with the assumption of local isotropy, could be slightly underestimated requiring a higher value of c_ε at **A1** to account for this "loss". The effectiveness of shear production of turbulence and the level of its isotropy in rotating oscillatory flows compared to unidirectional flows is a problem for further theoretical and experimental investigation.

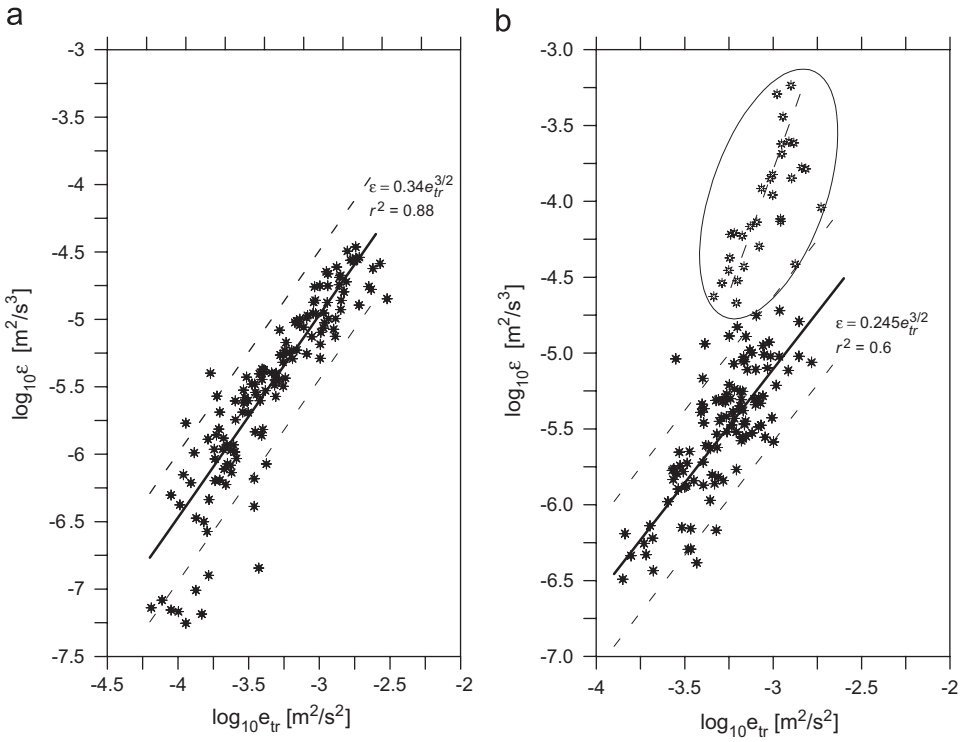

Fig. 11. The regression plots of the dissipation rate ε versus the turbulent kinetic energy e_{tr} at St. **D** (a) and **A1** (b). The approximations (heavy lines) are bounded by 95% confidence limits (dashed lines). The circled samples in (b) are presumably affected by convective mixing; the power fit in (b) is applied only for the filled circles ($\log_{10}\varepsilon < 4.7$).

6. Summary

In this study, we analyzed tidal-driven motions along the coast of China in the ECS (the Yellow Sea) focusing on the influence of barotropic tide on small-scale dynamics in the BBL. Measurements were conduced using bottom-mounted ADV and ADCP at a shallow-depth (19 m St. **D**) and at the sloping shelf (38 m depth St. **A1**). The testing sites were subjected to rotating (**A1**) and reversing (**D**) semidiurnal barotropic tidal flows. The logarithmic boundary layer at St. **A1** extended to ~8–10 mab and St. **D** to ~4–5 mab.

The kinetic energy dissipation rate near the bottom ε_{nb} was calculated using the inertial subrange of ADV vertical velocity spectra (Eqs. (1a) and (1b); Figs. 2 and 3). The results generally followed the variations of flow magnitude (or the turbulent Reynolds number Re_{nb}). At St. **D**, the highest $\varepsilon_{nb} \sim 5 \times 10^{-5}$ W/kg at $\zeta = 0.45$ mab was associated with the tidal flooding and the lowest $\varepsilon_{nb} \sim 10^{-7}$ W/kg with ebbing. A periodic increase of ε_{nb} during the ebb tide, with a period of ~2 h (Fig. 4), was consistent with the notion that the tidal flow was modulated by seiching of nearby Jiaozhou Bay (see Lozovatsky et al., 2007 for details). The near-bottom diffusivity K_{nb} at St. **D** was $\sim 3 \times (10^{-4}$–$10^{-3})$ m^2/s, which is about an order of magnitude larger than that observed on non-tidal shelves (Lozovatsky and Fernando, 2002).

In rotating flow at St. **A1**, ε_{nb} ($\zeta = 0.95$ mab) does not always correlate with tidally induced variations of Re_{nb}, but also depends on the change of flow direction. A substantial increase of ε_{nb} was found when the tidal current turned from the upslope to down-slope advecting warmer water from the east-northeast to the testing site along the seabed (Fig. 5), which may trigger convective mixing and enhance dissipation above the level associated with pure bottom friction. This hypothesis is supported by the maxima of vertical velocity spectra $E_w(f)$ that occur at $f \approx 2$–4 Hz during the "convection episodes" (Fig. 3). These spectral maxima can be attributed to small-scale elements with spatial scales of several centimeters (such as thermals and plumes) associated with convection.

The friction velocity u_* was calculated using the log-layer profiles (ADCP-based $u_{*(\log)}$) and the near-bottom covariance measurements (ADV-based $u_{*(\mathrm{cor})}$). In the reversing tidal current on a shallow shelf with relative thin (less than 4–5 mab) logarithmic layer, both estimates of friction velocity were well correlated, particularly during the periods of unidirectional flood flow (Fig. 6). The drag coefficient $C_d = u_{*(\mathrm{cor})}^2 / U^2$ in this case is approximately constant, close to its median value 1.65×10^{-3}. When the tidal flow rotates over a deeper sloping bottom exhibiting a thick logarithmic-like layer (~10 mab on the average), the log-layer $u_{*(\log)}$ was approximately twice the skin-layer $u_{*(\mathrm{cor})}$ (Fig. 8). The inapplicability of classical log-layer formulation (Eq. (2)) to the rotating tidal flow at St. **A1** due to possible influence of the form drag may be responsible to the observed disparity. The form drag can enhance $u_{*(\log)}$ approximately two times during specific phases when the

flow is directed toward asymmetric sand ripples or similar irregularities of the sloping bathymetry. It is also shown (Fig. 9) that the use of the full momentum balance equations (Eqs. (3) and (5)) for rotating tidal flow in order to estimate the characteristic values of friction velocities in a ~10 mab BBL leads to u_* which about two times larger than the skin-layer $u_{*(\mathrm{cor})}$. We concluded that the assumption of constant momentum flux that is used to calculate $u_{*(\log)}$ based on Eq. (2) is irrelevant (even during short periods) for energetic rotating tidal currents producing the BBL of variable height ($H_l = 6$–15 mab), which was observed at St. **A1**.

The validation of $u_{*(\mathrm{cor})}$ rather than $u_{*(\log)}$ as the friction velocity of the constant flux boundary layer results from our analysis of the relationship between ε_{nb} and $u_{*(\mathrm{cor})}$, which must obey the law of the wall (Eq. (2)). The classical dissipation parameterization (Eq. (6)) appears to be valid for the reversing tidal flow at St. **D** and perhaps to a lesser extent for the rotating tidal flow at St. **A1**. The question remains, whether the near-bottom turbulence in rotating tidal flow can be roughly described by the low of the wall with a higher constant of proportionality ($c_0 = 1.5$), or this is resulting from insufficient statistics and uncertainties of measurements and data processing. Weak stratification in the BBL and possible higher level of anisotropy of near-bottom turbulence are likely sources of the observed increase of c_0.

During the periods of combined influence of the bottom stress and convective mixing on the near-bottom dissipation rate, the deviation of the law of the wall is found to be substantial (Figs. 10b and 11b). The advection of warm bottom water from the northeast appears to cause near-bottom convection during a part of tidal cycle at St. **A1**. During these episodes, the dissipation and friction velocity does not follow the law of the wall and the dissipation increases substantially, which should affect sediment and bio-chemical transports in the region due to the patchiness of the near-bottom temperature in coastal waters of ECS. Identification of dominant processes and their spatial and temporal variability are of great importance in parameterizing turbulence and mixing in shelf waters dominated by tides.

Acknowledgments

The cruises were organized by Ocean University of China in Qingdao. We wish to thank scientists and students of OUC who participated in the measurements and data collection and the crew of R/V Dongfanghong-2. We appreciate help of Dr. Erofeeva from Oregon State University for making calculations of the components of the momentum balance equations at St. **A1** using the newest version of the OTIS software-TPXO7.1. The financial support was provided to the first and fourth authors by the US Office of Naval Research (Grant N00014-05-1-0245), and to the second and third authors by the Major State Program of China for Basic Research (Grant no. 2006CB400602), and the National Foundation of China for Natural Science (Grant no. 40490260). Comments of two anonymous reviewers were of help.

References

Beardsley, R.C., Duda, T.F., Lynch, J.F., Ramp, S.R., Irish, J.D., Chiu, C.-S., Tang, T.Y., Yang, Y.J., 2004. Barotropic tide in the northeast South China Sea. IEEE Journal of Oceanic Engineering 29, 1075–1086.

Businger, J.A., Wyngaard, J.A., Isumi, Y., Bradley, E.F., 1971. Flux profile relationships in the atmospheric surface layer. Journal of Atmospheric Science 28, 181–189.

Cheng, R.T., Ling, C.H., Gartner, J.W., 1999. Estimates of bottom roughness length and bottom shear stress in South San Francisco Bay, California. Journal of Geophysical Research—Oceans 104 (C4), 7715–7728.

Chriss, T.M., Caldwell, D.R., 1982. Evidence for the influence of form drag on bottom boundary layer flow. Journal of Geophysical Research—Oceans 87, 4148–4154.

Dewey, R.K., Crawford, G.B., 1988. Bottom stress estimates from vertical dissipation rate profiles on the continental shelf. Journal of Physical Oceanography 18 (8), 1167–1177.

Dillon, T.M., 1982. Vertical overturns: a comparison of Thorpe and Ozmidov scales. Journal of Geophysical Research—Oceans 87 (C12), 9601–9613.

Doron, P.K., Bertuccioli, L., Katz, J., Osborn, T.R., 2001. Turbulence characteristic and dissipation estimates in the coastal ocean bottom boundary layer from PIV data. Journal of Physical Oceanography 31 (8), 2108–2134.

Egbert, G.D., Erofeeva, S.Y., 2002. Efficient inverse modeling of barotropic ocean tides. Journal of Atmospheric and Oceanic Technology 19 (2), 183–204.

Elliott, A.J., 2002. The boundary layer character of tidal currents in the Eastern Irish Sea. Estuarine, Coastal and Shelf Science 55, 465–480.

Eriksen, C.C., 1982. Observations of internal wave reflection off sloping bottoms. Journal of Geophysical Research 87 (C1), 525–538.

Foster, D.L., Beach, R.A., Holman, R.A., 2000. Field observations of the wave bottom boundary layer. Journal of Geophysical Research—Oceans 105 (C8), 19634–19647.

Friedrichs, C.T., Hamrick, J.M., 1996. Effects of channel geometry on cross sectional variations in along channel velocity in partially stratified estuaries. Coastal and Estuarine Studies 53, 283–300.

Friedrichs, C.T., Wright, L.D., 1997. Sensitivity of bottom stress and bottom roughness estimates to density stratification, Eckernford Bay, southern Baltic Sea. Journal of Geophysical Research—Oceans 102 (C3), 5721–5732.

Fugate, D.C., Chant, R.J., 2005. Near-bottom shear stresses in a small, highly stratified estuary. Journal of Geophysical Research—Oceans 110 (C3).

Green, M.O., 1992. Spectral estimates of bed shear stress at subcritical Reynolds numbers in a tidal boundary layer. Journal of Physical Oceanography 22, 903–917.

Guo, X., Yanagi, T., 1998. Three-dimensional structure of tidal current in the East China Sea and the Yellow Sea. Journal of Oceanography 54 (6), 651–668.

Howarth, M.J., Souza, A.J., 2005. Reynolds stress observations in continental shelf seas. Deep-Sea Research II 52 (9–10), 1075–1086.

Kang, S.K., Foreman, M.G., Lie, H.-J., Lee, J.H., Cherniawsky, J., Yum, K.-D., 2002. Two-layer tidal modeling of the Yellow and East China Seas with application to seasonal variability of the M_2 tide. Journal of Geophysical Research 107, 3020, doi:10.1029/2001JC000838.

Kim, S.-C., Friedrichs, C.T., Maa, J.P.-Y., Wright, L.D., 2000. Estimating bottom stress in tidal boundary layer from Acoustic Doppler Velocimeter data. Journal of Hydraulic Engineering 126 (6), 399–406.

Kolmogorov, A.N., 1941. The local structure of turbulence in incompressible viscous fluid for very large Reynolds numbers. Doklady USSR Academy of Sciences 39, 301–305.

Li, M.Z., 1994. Direct skin friction measurements and stress partitioning over movable sand ripples. Journal of Geophysical Research—Oceans 99, 791–799.

Lorke, A., Umlauf, L., Jonas, T., Wüest, A., 2002. Dynamics of turbulence in low-speed oscillating bottom-boundary layers of stratified basins. Environmental Fluid Mechanics 2, 291–313.

Lozovatsky, I.D., Fernando, H.J.S., 2002. Turbulent mixing on a shallow shelf of the Black Sea. Journal of Physical Oceanography 32, 945–956.

Lozovatsky, I., Roget, E., Fernando, H.J.S., Figueroa, M., Shapovalov, S., 2006. Sheared turbulence in a weakly-stratified upper ocean. Deep Sea Research I 53, 387–407.

Lozovatsky, I.D., Liu Zhiyu, Wei Hao, Fernando, H.J.S., 2007. Tides and mixing in the northwestern East China Sea. Part I: Rotating and reversing tidal flows. Continental Shelf Research, doi:10.1016/j.csr.2007.08.006.

Lueck, R.L., Lu, Y., 1997. The logarithmic layer in a tidal channel. Continental Shelf Research 17, 1785–1801.

MacKinnon, J.A., Gregg, M.C., 2005. Spring mixing: turbulence and internal waves during restratification on the New England shelf. Journal of Physical Oceanography 35, 2425–2443.

Mellor, G.L., Yamada, T., 1982. Development of a turbulence closure model for geophysical fluid problems. Reviews of Geophysics and Space Physics 20, 851–875.

Monin, A.S., Yaglom, A.M., 1971. Statistical Fluid Mechanics: Mechanics of Turbulence, 1. MIT Press, Cambridge, MA, 782pp.

Monin, A.S., Yaglom, A.M., 1975. Statistical Fluid Mechanics: Mechanics of Turbulence, 2. MIT Press, Cambridge, MA, 874pp.

Moum, J.N., Perlin, A., Klimak, J.M., Levine, M.D., Boyd, T., Kosro, P.M., 2004. Convective driven mixing in the bottom boundary layer. Journal of Physical Oceanography 34, 2189–2202.

Perlin, A., Moum, J.N., Klymak, J.M., Levine, M.D., Boyd, T., Kosro, P.M., 2005. A modified law-of-the-wall applied to oceanic bottom boundary layers. Journal of Geophysical Research 110 (C10) Art. No. C10S10.

Sanford, T.S., Lien, R.-C., 1999. Turbulent properties in a homogeneous tidal boundary layer. Journal of Geophysical Research-Oceans 104 (C1), 1245–1257.

Shaw, W.J., Trowbridge, J.H., Williams, A.J., 2001. Budgets of turbulent kinetic energy and scalar variance in the continental shelf bottom boundary layer. Journal of Geophysical Research-Oceans 106 (C5), 9551–9564.

Smith, J.D., McLean, S.R., 1977. Spatially averaged flow over a wavy surface. Journal of Geophysical Research—Oceans 82, 1735–1746.

Smith, W., Nimmo, A.M., Katz,, J., Osborn,, T.R., 2005. On the structure of turbulence in the bottom boundary layer of the coastal ocean. Journal of Physical Oceanography 35 (1), 72–93.

Souza, A.J., Howarth, M.J., 2005. Estimates of Reynolds stress in highly energetic shelf sea. Ocean Dynamics 55, 490–498.

Sreenivasan, K.R., 1993. On the universality of the Kolmogorov constant. Physics of Fluids 7 (11), 2778–2784.

Stapleton, K.R., Huntley, D.A., 1995. Seabed stress determination using the inertial dissipation method and the turbulent kinetic energy method. Earth Surface Processes and Landforms 20 (9), 807–815.

Strang, E.J., Fernando, H.J.S., 2001. Entrainment and mixing in stratified shear flows. Journal of Fluid Mechanics 428, 349–386.

Telford, J.W., Businger, J.A., 1986. Comments on ''Von Karman's constant in atmospheric boundary layer flow: reevaluated''. Journal of the Atmospheric Sciences 43 (19), 2127–2130.

Testik, F.Y., Voropayev, S.I., Balasubramanian, S., Fernando, H.J.S., 2006. Self-similarity of asymmetric sand-ripple profiles formed under nonlinear shoaling waves. Physics of Fluids 10, 108101.

Thorpe, S.A., 1977. Turbulence and mixing in a Scottish Loch. Philosophical Transactions of Royal Society A 286, 125–181.

Thorpe, S.A., 1987. On the reflection of a train of finite-amplitude internal waves from a uniform slope. Journal of Fluid Mechanics 178, 279–302.

Thorpe, S.A., 2005. The Turbulent Ocean. Cambridge University Press, Cambridge, 485pp.

Voulgaris, G., Trowbridge, J.H., 1998. Evaluation of the Acoustic Doppler Velocimeter (ADV) for turbulence measurements. Journal of Atmospheric and Oceanic Technology 15 (1), 272–289.